Supporting Information

Quantification of efficient plasmonic hot-electron injection in gold nanoparticle – TiO_2 films

Daniel C. Ratchford,[1] Adam D. Dunkelberger,[1] Igor Vurgaftman,[2] Jeffrey C. Owrutsky,[1] and Pehr E. Pehrsson[1]*

[1]Chemistry Division and [2]Optical Sciences Division, US Naval Research Laboratory, Washington, D.C. 20375

*Corresponding author email: daniel.ratchford@nrl.navy.mil

Sample fabrication

Sapphire substrates were first cleaned in an isopropyl alcohol bath with sonication for 5 minutes. The substrates were blown dry with N_2, and then exposed to an O_2 plasma for 1 minute to remove any organic residue. Atomic layer deposition (Oxford Systems ALD system) was used to deposit TiO_2 and Al_2O_3 films onto different substrates. For the TiO_2 films, a tetrakis(dimethylamino)titanium precursor was used with a deposition rate of 0.5 – 0.7 $\text{Å}/cycle$. A 200 cycle deposition resulted in a thin ~13 nm layer of TiO_2. For the Al_2O_3 films, a trimethylaluminum precursor was used with a deposition rate of 1.2 -1.4 $\text{Å}/cycle$. A 150 cycle deposition resulted in a ~20 nm layer of Al_2O_3. The layer thickness was chosen to roughly match the Au interparticle distance within the Au NP layers. After the ALD deposition, Au was deposited on the samples using an electron beam evaporator (Temescal FC-2000) with a deposition rate of ~0.5 $\text{Å}/s$. The Au was deposited to a nominal thickness of 2 nm, as measured by a quartz crystal microbalance. The samples were then annealed at 500 ºC under an N_2 environment for 5 minutes. The deposition and annealing process results in small, separated islands of Au with dimensions on the order of 10 nm. This process of ALD film deposition followed by deposition of Au islands was then repeated on each sample 4 more times to create stacks of either TiO_2-Au or Al_2O_3-Au, with 5 total layers of Au islands. As a final step, another layer of TiO_2 (Al_2O_3) was deposited on the TiO_2-Au (Al_2O_3-Au) stacks to fully embed the last layer of Au islands. The final total thickness of the TiO_2-Au (Al_2O_3-Au) stack was approximately 90 nm (130 nm). A control sample consisting of a TiO_2 film without Au NPs was also made by depositing 1200 cycles of ALD TiO_2 on a clean sapphire substrate, yielding a TiO_2 film with a thickness of ≈70 nm. Additional samples were made simultaneously on silicon

witness coupons in order to image the samples with an SEM. SEM images, supplemented by ellipsometry, were used to determine the ALD deposition rate and the film thicknesses. Raman scattering measurements were performed on the TiO_2-only film and suggest that the TiO_2 has anatase crystallinity.

SEM image of TiO_2-Au sample on a sapphire substrate

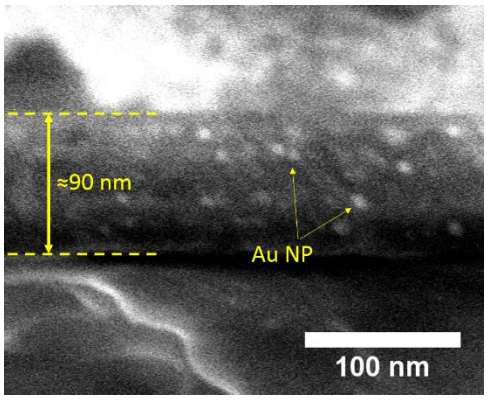

Figure S1 Side-view SEM image of TiO2-Au sample on sapphire substrate.

Although charging prevented capturing sharp SEM images of the samples on the sapphire substrates, Figure S1 shows a cross-sectional SEM image of the TiO_2-Au sample on sapphire. The sapphire substrate is located at the bottom of the image, and the TiO_2-Au layer is between the yellow dashed lines. From the image, one can see that the TiO_2-Au layer is approximately 90 nm.

Optical characterization

Steady state optical spectra from the TiO_2-only film, TiO_2-Au stacks, and Al_2O_3-Au stacks were acquired with a Perkin-Elmer Lambda 1050 spectrometer equipped with an integrating sphere to measure the total transmission, T, and reflection, R. These measurements

account for diffuse scattering from the sample. The absorption, A, of each sample is given by A = 1-T-R.

Transient absorption measurements were performed using a regeneratively amplified Ti:Sapphire laser (wavelength = 800 nm and repetition rate = 1 kHz) which pumps two independently tunable optical parametric amplifiers (OPA). The pump beam wavelength varied with experiment, and the wavelengths are noted within the discussion. The frequency-doubled output (for visible pump and quadrupled for UV pump) from one OPA was used to produce the pump beam while the other OPA produced the probe either via second harmonic generation for visible probe or difference frequency generation for infrared probe at 5 μm. The typical pump beam spot size was ≈400 μm, and the probe beam was slightly smaller. The probe beam passed through a delay stage to change the time delay between the pump and the probe pulses. Independent lenses focused the pump and probe beams onto the sample at a small angle. A lock-in amplifier was referenced to a chopper that modulated the pump laser and was used to measure pump-induced changes to the intensity of the transmitted probe light. Changes in the probe transmission through the samples were detected with a mercury-cadmium-telluride photodetector for the infrared probe pulses and a Si photodiode for the visible probe pulses.

Absorption spectra calculations of the TiO_2-Au and Al_2O_3-Au samples

In order to qualitatively understand the static absorption spectra from the TiO_2-Au and Al_2O_3-Au samples, we used the Maxwell Garnett effective medium approximation to estimate an effective permittivity for each thin film sample and calculated the spectra using Fresnel equations. Under the Maxwell Garnett effective medium approximation, the permittivity of a medium consisting of a matrix medium with permittivity ε_m embedded with spherical inclusions with permittivity ε is given by

$$\varepsilon_{eff} = \varepsilon_m \left(1 + \frac{3f\left(\frac{\varepsilon - \varepsilon_m}{\varepsilon + 2\varepsilon_m}\right)}{1 - f\left(\frac{\varepsilon - \varepsilon_m}{\varepsilon + 2\varepsilon_m}\right)} \right) \qquad (S1)$$

where f is the volume fraction of the inclusions.

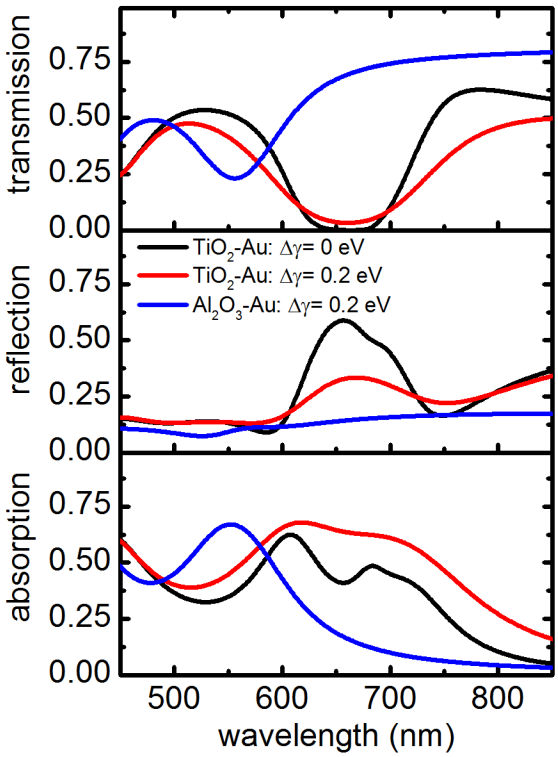

Figure S2 Calculated transmission, reflection, and absorption of the TiO_2-Au sample (black and red curves) and the Al_2O_3-Au sample (blue curve) based on Eq. S1.

The black curves in Figure S2 a, b, and c (above image) show the calculated transmission, reflection, and absorption for the TiO_2-Au sample using Eq. S1 to estimate the effective permittivity. The calculations were carried out using the ellipsometry software WVASE and assume normal incident light on a 90 nm thick TiO_2-Au layer on top of a 0.5 mm thick sapphire substrate. To approximate the permittivity of the TiO_2-Au, we let $\varepsilon_m = 6.25$ (n = 2.5) for the TiO_2 matrix, and we used an analytical

function for the dielectric function of gold from the work of Vial et al.[1] The function consists of the typical Drude term for a metal with an additional Lorentzian term to account for interband transitions:

$$\varepsilon(\omega) = \varepsilon_\infty - \frac{\omega_D^2}{\omega^2 + i\omega\gamma_D} - \frac{\Delta\varepsilon \cdot \omega_L}{\omega^2 - \omega_L^2 + i\omega\gamma_L} \qquad (S2)$$

Here, ε_∞ is the high frequency permittivity, ω_D is the plasma frequency, γ_D is the Drude damping coefficient, and $\Delta\varepsilon$, ω_D, and $\gamma_D$are the weight parameter, oscillator strength, and damping coefficient for the Lorentzian term. For each of these parameters, we used values determined by Vial et al. for an optimal fit to the Johnson and Christy measured optical constants of gold from 500 to 1000 nm.[1] These values are listed in the table below. For the gold volume fraction, we used f = 0.08, which was chosen to closely match the gold volume fraction estimated from the SEM images.

ε_∞	ω_D (eV)	γ_D (eV)	$\Delta\varepsilon$ (eV)	ω_D (eV)	γ_D (eV)
5.9673	8.74	0.066	1.09	2.69	0.43

The calculated spectra have many of the same spectral features as the measured in the static spectra from Figure 2. There is a strong transmission dip and reflection peak centered on ≈650 nm, and the absorption spectrum is very broad, spanning from about 550 nm to 800 nm with a spectral dip around 650 nm. However, overall the spectral features have narrower bandwidths compared to the experimental data. The additional broadening of the experimental data could be the result of the random aspect ratio of the Au NPs or from the well-known effect of surface damping. Surface damping occurs in small NPs with diameters less than the mean free path of the conduction electrons and results in an increase in the electron scattering rate.[2] While we did not determined the exact nature of the additional broadening in these samples, we can account for it in the calculations by modification of the Drude damping term. The Drude damping term is replaced with

$$\gamma = \gamma_D + \Delta\gamma \tag{S3}$$

where the parameter $\Delta\gamma$ accounts for the additional broadening. In Figure S2, the red curves are calculated the same way as the black curves but with the Drude damping term replaced with Eq. S3. We found that letting $\Delta\gamma$ = 0.2 eV results in a calculated spectrum that closely matches the experimental data.

The above permittivity model works well for calculating the Al_2O_3-Au spectra as well. The blue curves in Figure S2 show the calculated spectra for a dielectric matrix with a permittivity value of similar to that of Al_2O_3: $\varepsilon_m = 2.89$ (n = 1.7). For this calculation, the layer thickness was 130 nm, $\Delta\gamma$ = 0.2 eV and f = 0.06 in order to match the volume fraction of the Al_2O_3-Au sample. The reduced volume fraction compared to the TiO_2-Au sample is due to its larger overall sample thickness. One can see that the change in the matrix index results in a plasmon resonance which is centered around 550 nm, similar to the experimental data.

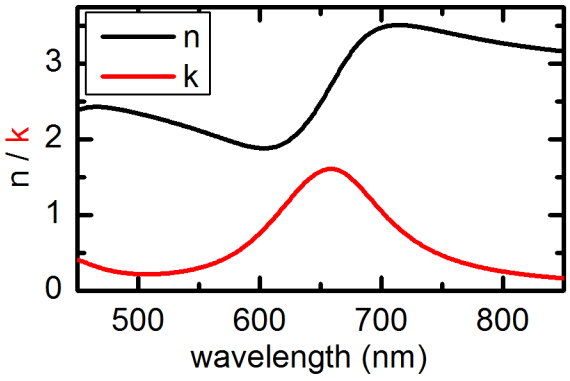

Figure S3 The effective optical constants, *n* and *k*, of the TiO_2-Au film used to calculate the spectra (red curves) in Figure S2.

A noteworthy feature of the TiO_2-Au absorption spectrum (red curve in Figure S2c) is the dip around 650 nm. In order to see why this dip arises, the effective TiO_2-Au optical constants used to calculate the red curve in Figure S2c are shown in Figure S3. One can see a sharp rise in the refractive index *n* from 600 nm to 700 nm, which results in increased reflection over this spectral region, thus, resulting in dip in the absorption spectrum.

Photoluminescence from TiO_2 and plasmon enhancement of sub-bandgap transitions

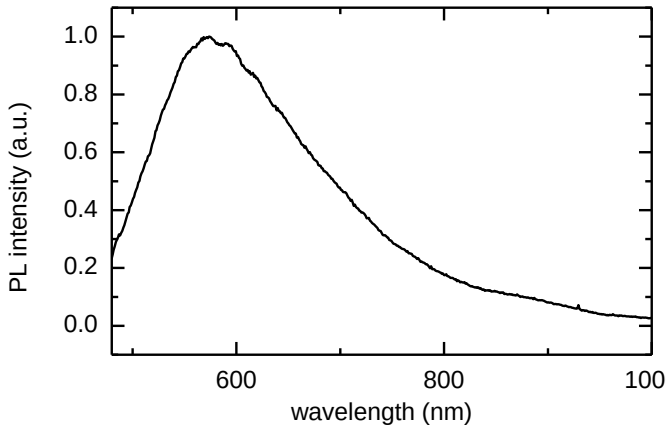

Figure S4 Photoluminescence from the TiO_2-only film.

The TiO_2-only film exhibits very weak photoluminescence (PL). Figure S4 shows the PL from the TiO_2-only thin film sample with laser excitation at $\lambda = 443nm$. A long pass filter with a cutoff at 480 nm was placed in the emission path to filter out the excitation light. The broad PL spectrum centered at ≈600 nm is similar to previously reported emission spectra from anatase TiO_2 and has been attributed to a variety of defects including oxygen vacancies and under-coordinated Ti atoms.[3-6]

Besides charge injection, one possible origin for the mid-IR transient absorption signal of the TiO_2-Au sample (Figure 3b, red curve) is the excitation of the TiO_2 sub-bandgap transitions. Any process which promotes electrons into the TiO_2 conduction band (including excitation of sub-bandgap transitions) would generate a mid-IR transient absorption signal if the excited carrier density is sufficiently high. As we discuss in the manuscript, we used the TiO_2-only film as a control to verify that excitation of the sub-bandgap transition does not contribute to the signal around the plasmon resonance. However, the presence of the plasmonic field might enhance excitation of sub-bandgap transitions, potentially leading to a detectable signal. The mid-IR transient absorption measurement by itself is not capable of determining the mechanism by which electrons are promoted into the TiO_2 conduction band. In the manuscript, the Au electron dynamics are shown to corroborate the charge injection model from the Au NPs. Furthermore,

the magnitude of the charge injection estimated from the Au NP electron dynamics is in agreement with mid-IR transient absorption results. It is the agreement between these two datasets that implies that charge injection is the dominate process resulting in the promotion of electrons into the TiO_2 conduction band.

TiO_2-Au transient IR-absorption peak below 500nm

In Figure 3c, the maximum IR amplitude, ΔA_{max}, from the TiO_2-Au stack is plotted as a function of pump wavelength, and while the signal tracks the plasmon band, there is an additional peak around 450 nm. The TiO_2-Au absorption spectrum has a small spectral peak in this region, but overall, is relatively flat compared to the plasmon band. We did not fully resolve the origin of this secondary carrier injection peak, but below we discuss a few different possibilities.

First, the spectral peak may result from the excitation of d-band electron from the Au NPs that are then injected into the TiO_2. The onset of the gold d-bands is ≈ 2 eV (λ ≈ 600 nm) below the Fermi level. Therefore, the d-band absorption should dominate at a pump wavelength of 450 nm. For a photon energy of 2.75 eV corresponding to this wavelength, the maximum energy of the excited d-band electrons is ≈ 0.75 eV above the Fermi level, near the previously reported TiO_2-Au interfacial energy barrier heights of 0.9-1.2eV. Therefore, if the barrier height is slightly lower than previously reported, electrons excited from the d-band may cross the interfacial barrier, resulting in an increase in transient IR absorption signal. However, if this mechanism were significant, one would expect comparable absorption at 450 nm to the plasmon band peak. Since this is not observed, it appears that the barrier height is sufficient to filter out the electrons excited from the d-band.

A second possibility is that the additional transient signal originates from excitation of electrons into the TiO_2 conduction band from TiO_2 trap states. We know that TiO_2 trap states are present from the PL data presented above as well as from the absorption spectra shown in Figure 2c. Excitation of trapped electrons to the conduction band may occur either through direct excitation or possibly by absorption in the Au NP followed by the excitation of trapped electrons through a dipole-dipole coupling process. The

peaked nature of the response at 450 nm leads us to suspect that the signal is related to the excitation of trapped electrons. However, we cannot strictly rule out the possibility that the increase is related to the excitation of d-band electrons.

Probability of tunneling from Au NPs into the TiO_2

We can use values from the literature to estimate the probability of electron tunneling from the Au NPs into the TiO_2. In general, the probability of tunneling depends exponentially on the barrier height and width. In the case of the TiO_2-Au NP system, we can approximate the band bending at the metal-semiconductor interface as a triangular barrier, with a height equal to the Schottky barrier height (≈1 eV) and the leg of the triangular barrier to be the depletion layer width. The depletion width at a metal-semiconductor interface is approximately

$$W = \sqrt{\frac{2\varepsilon V}{qN}}$$

where ε is the dielectric constant of the semiconductor, V is the built-in potential measured from the top of the barrier to the top of the semiconductor conduction band ($V \approx 1$ eV for the TiO_2-Au interface), q is the electron charge, and N is the ionized impurity density.[7] The dielectric constant for anatase TiO_2 is about $30\varepsilon_0$, where ε_0 is the vacuum permittivity.[8] Using a conservative estimate for $N = 10^{18}$ cm^{-3} yields a depletion layer width of about 58 nm.

The transmission probability to penetrate a certain distance, l, through a triangular barrier is given by

$$T = \exp\left(-2\int_0^l \sqrt{\frac{2m}{\hbar^2}\left(\phi\left(1-\frac{x}{W}\right)\right)}\,dx\right)$$

where *m* is the electron mass and ϕ is the barrier height (ϕ ≈ 1 eV for the TiO_2-Au interface).[7] Even with a depletion width of 10 nm, the tunneling probability into the TiO_2 is negligible. Therefore, tunneling is not expected to contribute to the charge injection results.

Transport probability

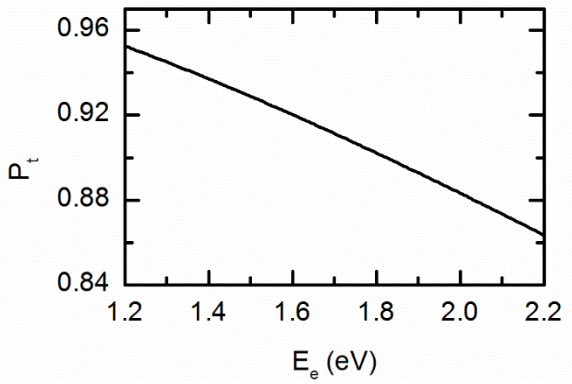

Figure S5 shows Eq. 2 evaluated for a 10 nm NP.

References

1. Vial, A.; Grimault, A. S.; Macías, D.; Barchiesi, D.; Lamy De La Chapelle, M. *Phys. Rev. B* **2005,** 71, (8), 085416.
2. Kreibig, U.; Vollmer, M., *Optical Properties of Metal Clusters*. Springer: 1995; Vol. 25.
3. Chang, Y. H.; Liu, C. M.; Chen, C.; Cheng, H. E. *J. Electrochem. Soc.* **2012,** 159, (7), D401-D405.
4. Jin, C.; Liu, B.; Lei, Z.; Sun, J. *Nanoscale Res. Lett.* **2015,** 10, (1), 95.
5. Knorr, F. J.; Mercado, C. C.; McHale, J. L. *J. Phys. Chem. C* **2008,** 112, (33), 12786-12794.
6. Ohta, S.; Sekiya, T.; Kurita, S. *Phys. Status Solidi B* **2001,** 223, (1), 265-269.
7. Sze, S. M., *Physics of Semiconductor Devices*. Second ed.; John Wiley & Sons: New York, 1981.
8. Roberts, S. *Phys. Rev.* **1949,** 76, (8), 1215-1220.